Materials Advances

ROYAL SOCIETY OF CHEMISTRY

PAPER

View Article Online
View Journal | View Issue

Cite this: *Mater. Adv.*, 2024, 5, 4345

In situ growth of $NiSe_2$ nanoparticles on g-C_3N_4 nanosheets for an efficient hydrogen evolution reaction†

Somnath R. Khaladkar,[a] Oshnik Maurya,[a] Girish Gund,[b] Bhavesh Sinha,[c] Girish Kamble,[d] Jin Hyeok Kim, *[d] R. R. Deshmukh*[a] and Archana Kalekar *[a]

Received 1st November 2023,
Accepted 25th March 2024

DOI: 10.1039/d3ma00948c

rsc.li/materials-advances

A safe, non-precious, and low-cost catalyst, having a high hydrogen evolution rate, is one of the key demands for a sustainable hydrogen economy. In this study, we used a low-cost hydrothermal technique to prepare a $NiSe_2$ nanoparticle-based catalyst. These particles were grown on 2D g-C_3N_4 nanosheets to improve their physical and chemical properties. The synthesized $NiSe_2$/g-C_3N_4 nanocomposite catalyst demonstrated a high HER performance when compared to bare $NiSe_2$ and g-C_3N_4. Specifically, the $NiSe_2$/g-C_3N_4 composite demonstrated a lower Tafel slope of 64 mV dec^{-1}, a stable HER up to 1000 min, and a low overpotential of 87 mV at a current density of 10 mA cm^{-2}. The superior HER performance of the composite on 2D g-C_3N_4 corresponds to high active sites, and the synergistic interfacial contact leads to enhanced conductivity for rapid charge transport and long chemical stability. Thus, our study offers a pathway for the synthesis and development of non-precious, non-toxic, and highly stable electrocatalysts to replace noble metal-based catalysts and reduce the production costs of H_2 gas.

1. Introduction

The depletion of fossil fuels and accompanying environmental damage, requires a search for a new and unconventional energy source.[1] Hydrogen has emerged as an optimal solution for tackling the escalating energy and environmental challenges faced globally. The energy density of hydrogen is about 140 MJ kg^{-1}, which is nearly three times that of gasoline (46.5 MJ kg^{-1}).[2] Hydrogen is produced using different technologies such as photolysis, electrolysis, or thermolysis. Electrocatalytic water splitting, one of the major energy study fields, has been under intense development by researchers to produce a high yield of H_2 gas with an acceptable energy and cost consumption. Using suitable electrocatalysts, the water splitting leads to the hydrogen evolution reaction (HER). An ideal electrocatalyst should increase the faradaic efficiency, speed up the reaction kinetics, reduce ohmic losses, and work in different pH conditions. Extensive research has revealed a wide range of electrocatalysts that catalyze these critical reactions. Currently, platinum (Pt) and Pt-based electrodes show a very high catalytic performance and stability for HER. However, their commercial application is constrained by their high price and limited availability. Overall, there is an urgent requirement to develop state-of-the-art, high-performance, non-precious metal-based electrocatalysts for electrocatalytic H_2 generation.[3–7]

Recently, earth-abundant[8] transition metal-based chalcogenides,[9] hydroxides, phosphides,[10] carbides, nitrides, metal–organic-frameworks (MOF),[11] are being investigated for their HER activities. The chalcogenides are anticipated to be more covalent, have smaller band gaps, and offer better band alignment with water redox levels than their counterparts, allowing for more effective charge transfer and improved catalytic efficiency. Among chalcogenides, nickel selenide ($NiSe_2$) exhibits a relatively superior electrochemical catalytic activity, chemical stability, low toxicity, and bio-compatibility. However, particle agglomeration and low electrical conductivity lead to a low HER performance because of the sluggish charge kinetics, which need to be resolved.[12,13]

Several strategies have been utilized to improvise the electrochemical activity of $NiSe_2$. Some examples include nanostructurization,[14] dual-anion doping,[15] doping,[16] interfacial

[a] *Department of Physics, Institute of Chemical Technology (ICT), Matunga, Mumbai, Maharashtra, 400019, India. E-mail: rr.deshmukh@ictmumbai.edu.in, s.kalekar@ictmumbai.edu.in, archanaphysics2017@gmail.com*
[b] *Department of Physics, M. P. A. S. C. College, Panvel, Maharashtra, 410206, India*
[c] *National Center for Nanoscience and Nanotechnology, University of Mumbai, Mumbai, Maharashtra, 400032, India*
[d] *Optoelectronics Convergence Research Center and Department of Material Sciences and Engineering, Chonnam National University, 200, Yongbong-Dong, Buk-Gu, Gwangju, 61186, South Korea. E-mail: jinhyeok@chonnam.ac.kr*

† Electronic supplementary information (ESI) available. See DOI: https://doi.org/10.1039/d3ma00948c

engineering.[16,17] In particular, 2D-based layered materials offer greater potential for different electrochemical applications.[18] Graphitic carbon nitride (g-C_3N_4) offers simple synthesis, excellent stability, a 2D layered structure, and a tunable molecular structure for heterogeneous electrocatalysts.[19,20] The g-C_3N_4 enhances the interaction with materials by providing N sites, resulting in abundant active sites, optimized electronic states, and rapid mass/charge transfer.[21,22]

Different research groups have utilized g-C_3N_4 to design heterostructures for enhancing the electrocatalytic HER activity. Guan *et al.* synthesized a MoS_2/g-CN heterostructure that demonstrated an overpotential of 141 mV at 10 mA cm^{-2} and a Tafel slope of 57 mV dec^{-1}.[23] In another report, Zulqarnain *et al.* $FeCoSe_2$/g-C_3N_4 was found to show an HER at an overpotential of 83 mV at 20 mA cm^{-2} and a current density of 14.80 mA cm^{-2} at 0 V (*vs.* RHE),[24] which was considerably greater when compared to bare $FeCoSe_2$. Other researchers studied g-C_3N_4/MoS_2,[25] holey g-C_3N_4 supported single-atom catalysts (SACs),[26] $FeSe_2$/g-C_3N_4,[27] MoB/g-C_3N_4,[28] C_3N_4@MoN,[29] g-C_3N_4/C,[30] $FeSe_2$/g-C_3N_4[31] and demonstrated the role of g-C_3N_4 in improving the HER properties of compounds. Thus, it is expected that hetero-structuring of g-C_3N_4 with $NiSe_2$ can effectively improve the electrochemical properties of $NiSe_2$ to give a high-performance HER.

Herein, we have grown $NiSe_2$ on g-C_3N_4 nanosheets to form a $NiSe_2$/g-C_3N_4 nanocomposite using a hydrothermal method. The N-sites of g-C_3N_4 during the hydrothermal process interacted synergistically with $NiSe_2$ to improve the electrical conductivity, active surface area, and charge kinetics. The prepared electrocatalyst exhibited excellent HER activity with a smaller overpotential of 87 mV to give a current density of 10 mA cm^{-2}, a reduced Tafel slope of 64 mV dec^{-1}, and a long-time stable HER activity up to 1000 min.

2. Experimental details

2.1. Materials

The high purity chemicals were utilized without further purification. Melamine, hydrazine hydrate, nickel(II) acetate tetrahydrate, and *N*-methyl-2-pyrrolidinone (NMP), selenium powder (Se), acetylene black and polyvinylidene fluoride (PVDF) were purchased from Sigma-Aldrich Chemical Reagent Co. Ltd.

2.2. Preparation of g-C_3N_4

Using a previously reported method,[32] bulk g-C_3N_4 was synthesized using the thermal polycondensation of melamine.[33,34] To achieve this, 5 g of melamine was heated in an alumina crucible under an air environment, until it gradually reached 550 °C (5 °C min^{-1}). After a 4 h heating period, the mixture was cooled naturally to room temperature and ground in a mortar, to form a yellow bulk g-C_3N_4 powder. It was then transferred to an alumina crucible and subjected to a heating process in a nitrogen environment. The temperature was raised to 500 °C (5 °C min^{-1})/2 h. Finally, the obtained mixture was cooled naturally to ambient temperature, resulting in the formation of light yellow layered g-C_3N_4 nanosheet powder.

2.3. Preparation of $NiSe_2$/g-C_3N_4

In a typical synthesis, an equal volume ratio of g-C_3N_4 nanosheets and deionized (DI) water was subjected to ultrasonication at room temperature for 1 h. The resulting solution was centrifuged at 2500 rpm/5 min, and the supernatant collected was a g-C_3N_4 nanosheet suspension. Next, a mixture was prepared by combining 2 mmol of nickel acetate, 2 mmol of selenium powder, and 20 mL of g-C_3N_4 nanosheet suspension (1 mg mL^{-1}) in 50 mL of DI water. The mixture was stirred (800 rpm) for 20 min followed by dropwise addition of 20 mL of hydrazine. The solution was introduced into a hydrothermal reactor with a volume of 100 mL and held at a temperature of 180 °C for 12 h. To eliminate containments, the resulting precipitate underwent multiple washings using DI water and ethanol. The deep-gray precipitate was collected and dried overnight in vacuum oven at 80 °C to produce the $NiSe_2$/g-C_3N_4 nanocomposite.[5]

2.4. Measurement of the catalytic activity towards the HER

The electrocatalytic properties of prepared materials were measured using a PGSTAT302N electrochemical workstation (Metrohm Autolab), in a three-electrode configuration at room temperature. The setup consists of Hg/HgO (reference), graphite rod (counter) and synthesized material (working) electrodes in an aqueous 1 M KOH electrolyte. The active electrode was prepared by drop-casting the active catalyst (2 mg) in 5 wt% Nafion (15 μL) and isopropanol (2 mL) onto the 1 × 1 cm^2 nickel foam (NF). Prior to the electrochemical analysis, cyclic voltammetry (CV) was carried out for 50 cycles in the potential window of 1 V to 1.6 V *vs.* RHE. The linear sweep voltammetry (LSV) curves acquired were adjusted using the iR compensation at a scan rate of 10 mV s^{-1}. Electrical impedance spectroscopy (EIS) was carried out in the frequency range of 1 MHz to 100 mHz, and chronoamperometry was carried out to measure the stability. The reversible hydrogen electrode (RHE) scale was utilized for standardizing LSV potential values using, E *vs.* RHE = E *vs.* Hg/HgO + 0.950 V. To compute the electrical double layer capacitance (C_{dl}), in the potential range of 0 to 0.2 V *vs.* RHE, the scan speeds in CV curves were varied from 5 to 50 mV s^{-1}.

2.5. Material characterization

The physicochemical characteristics of the synthesized materials were investigated using different characterization techniques. X-ray diffraction (XRD, Rigaku Ultima IV) using CuKα radiation (λ = 0.15406 nm) was used for the phase configuration and structural details. The field emission scanning electron microscopy (FE-SEM, Jeol JSM-7900F, Japan), was utilized for understanding surface morphological characteristics. A spectrophotometer (Bruker, USA) was used to perform Fourier transform infrared (FTIR) spectroscopy. Selected area electron diffraction (SAED) and high-resolution transmission electron microscopy (HR-TEM) were performed using a Jeol JEM-2200FS. A K-alpha+ X-ray spectrometer was used for the X-ray

photoelectron spectroscopy (XPS) investigation. The contact angles were measured with respect to standard liquids with a Rame-Hart goniometer.

3. Results and discussion

3.1. Reaction and growth mechanism

The possible reaction mechanism for the formation of $NiSe_2$ and $NiSe_2$/g-C_3N_4 was explained by chemical reactions. First, the ionic dissociation of nickel acetate in the reactant solution takes place (see eqn (1)). In the presence of the strong reducing agent, hydrazine hydrate, Ni^{2+} is reduced forming an intermediate complex (see eqn (2)). Moreover, the highly basic hydrazine hydrate and the temperature inside hydrothermal treatment promote the dissolution of the Se powder in DI water to form Se^{2-} and SeO_3^{2-} ions (eqn (3)). The used hydrazine hydrate controls the pH and release of the Se^{2-} ions. The used Ni : Se precursor ratio was 1 : 2, so the final product should be a diselenide. These Se^{2-} ions will react with the Ni complex to form $NiSe_2$ (the desired product, see eqn (4)).

$$Ni(CH_3CO_2)_2{\cdot}4HO \rightarrow Ni^{2+} + 2(CH_3CO_2)^- + 4H_2O \quad (1)$$

$$2Ni^{2+} + 6N_2H_4 + 4OH^- \rightarrow 2[Ni(N_2H_4)_3]^{2+} + 4OH^- \quad (2)$$

$$3Se + 6OH^- \rightarrow 2Se^{2-} + SeO_3^{2-} + 3H_2O \quad (3)$$

$$[Ni(N_2H_4)_3]^{2+} + 2Se^{2-} \rightarrow NiSe_2 + 6N_2H_4 \quad (4)$$

To form the composite, a similar procedure was used with addition of g-C_3N_4 during the hydrothermal treatment. The g-C_3N_4 nanosheets provide enormous active sites for $NiSe_2$ nanoparticles to grow. To reduce the reaction energy, these particles tend to aggregate which leads to self-assembly and anisotropic

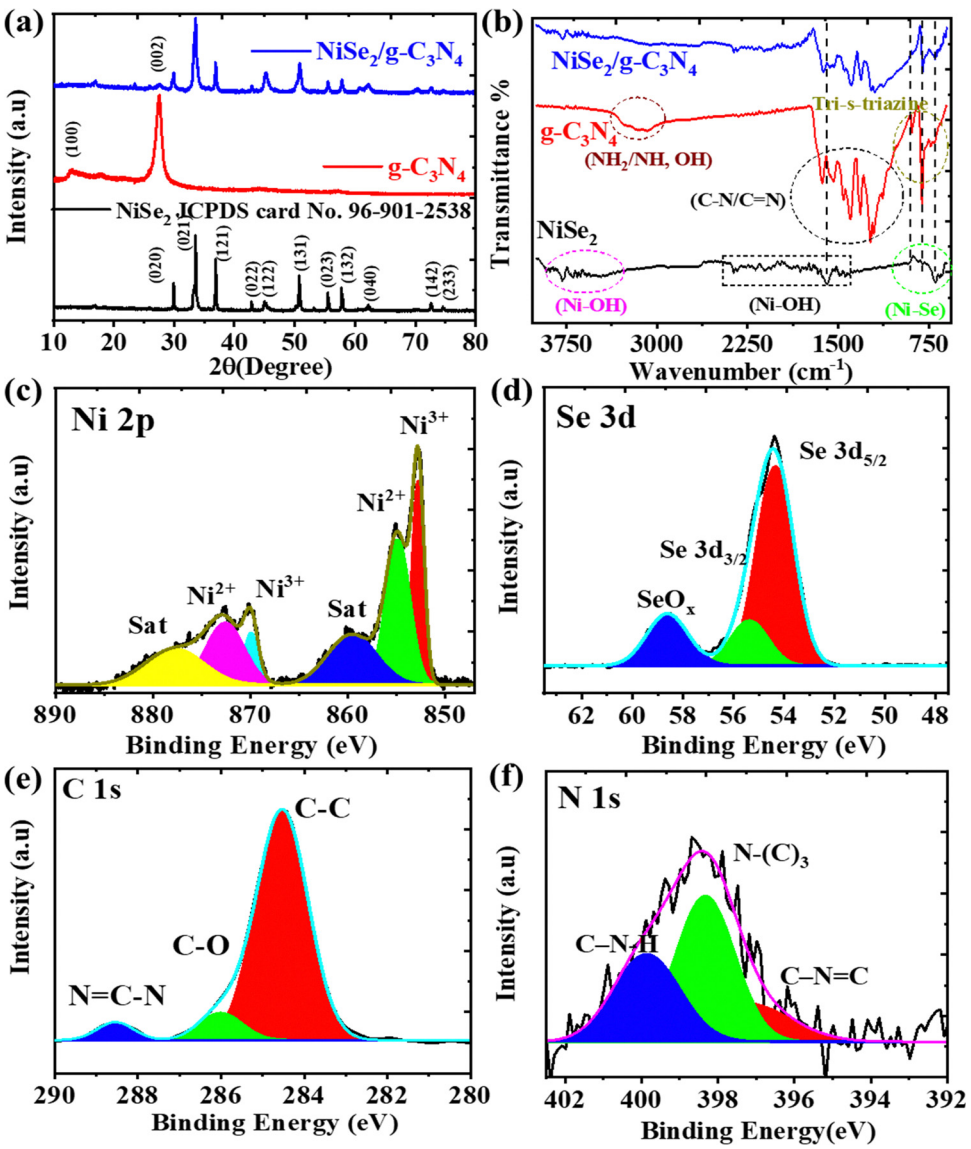

Fig. 1 (a) XRD and (b) FTIR patterns for the $NiSe_2$, g-C_3N_4, and $NiSe_2$/g-C_3N_4 nanocomposite. (c)–(f) XPS patterns of Ni 2p, Se 3d, C 1s, and N 1s in $NiSe_2$/g-C_3N_4 nanocomposite.

growth. The favorable surface and electronic charge distribution of g-C_3N_4 encourages the attachment of the $NiSe_2$ nanoparticles on its surface. The directed attachment process, the Gibbs–Thompson law, and the Ostwald ripening stabilize the chemical system, forming the $NiSe_2$/g-C_3N_4 composite.[35–38]

3.2. Material characterization

The crystal phase and structure of $NiSe_2$, g-C_3N_4, and $NiSe_2$/g-C_3N_4 were analyzed by X-ray diffraction (XRD). In the XRD pattern of g-C_3N_4 (Fig. 1(a)), a peak at 13.2° is related to the (100) plane that arose due to in-planar tri-*s*-triazine units, whereas another peak at 27.5° belonged to the (002) plane originating from the layer stacking arrangement of conjugated aromatic systems.[39] The XRD pattern of $NiSe_2$ reveals stronger intensity peaks at 2θ = 29.93°, 33.55°, 36.91°, 50.71°, and 57.79° corresponding to the crystal planes of (020), (021), (121), (131), and (132), respectively, which was confirmed from the standard card (JCPDS no. 96-901-2538).[40] The stronger peaks in the composite sample proved that the $NiSe_2$/g-C_3N_4 composite was successfully synthesized, and that there were no extra peaks. The peak positions of $NiSe_2$/g-C_3N_4 are consistent with $NiSe_2$, and a smaller peak of g-C_3N_4 at 27.5° was observed suggesting that the crystal structure remains unaffected in presence of g-C_3N_4. Using the Debye Scherrer equation, the calculated crystallite sizes for $NiSe_2$ and $NiSe_2$/g-C_3N_4 samples were 26.16 and 24.89 nm, respectively. Surface functionalities were studied using FTIR spectroscopy. The FTIR spectra of $NiSe_2$, g-C_3N_4, and $NiSe_2$/g-C_3N_4, are shown in Fig. 1(b). A peak at 801 cm^{-1} arose due to the characteristic absorption of the condensed heptazine heterocyclic (C_6N_7) ring in g-C_3N_4. The bending and stretching modes of N-containing heterocycles in g-C_3N_4 were characterized by the peak at 890 cm^{-1} and the absorption band in the range of 1000–1750 cm^{-1}, respectively. The broader peaks in 3000–3500 cm^{-1} range were related to –NH or $–NH_2$ groups in g-C_3N_4.[41] For $NiSe_2$, a broad band in the region of 500 to 900 cm^{-1} is attributed to the stretching vibrations of nickel–selenium bonds. The bending and stretching vibrations of adsorbed water on $Ni(OH)_2$ are responsible for bands observed at around 1600 cm^{-1} and 3600 cm^{-1}, respectively. Moreover, the adsorption peaks of $NiSe_2$/g-C_3N_4 are comprised of the respective peaks of $NiSe_2$ and g-C_3N_4, indicating the successful integration of the $NiSe_2$ nanoparticles on the g-C_3N_4 nanosheet.[42–48]

To investigate surface chemical states, XPS measurements were performed. Fig. S1a–c (ESI†) shows the XPS spectra of Ni 2p and Se 3d of $NiSe_2$. The Ni 2p spectrum contains Ni 2p1/2, Ni 2p3/2, and corresponding satellite peaks. The deconvoluted peaks of Ni^{2+} 2p1/2 of $NiSe_2$ and Ni^{2+} 2p1/2 of $Ni(OH)_2$ are located at 870 and 872.77 eV, respectively.[49] The other two deconvoluted peaks at 852.82 and 855.17 eV are related to the Ni^{2+} 2p3/2 of $NiSe_2$ and Ni^{2+} 2p3/2 of $Ni(OH)_2$. The surface absorption of water may be responsible for the occurrence of the deconvoluted peaks of Ni^{2+} 2p of $Ni(OH)_2$.[50] The peaks at 860 and 880.15 eV correspond to standard Ni 2p satellite peaks.

Fig. S1d–f (ESI†) shows XPS survey spectra and the deconvolution curves for the g-C_3N_4 sample. The C 1s XPS spectra

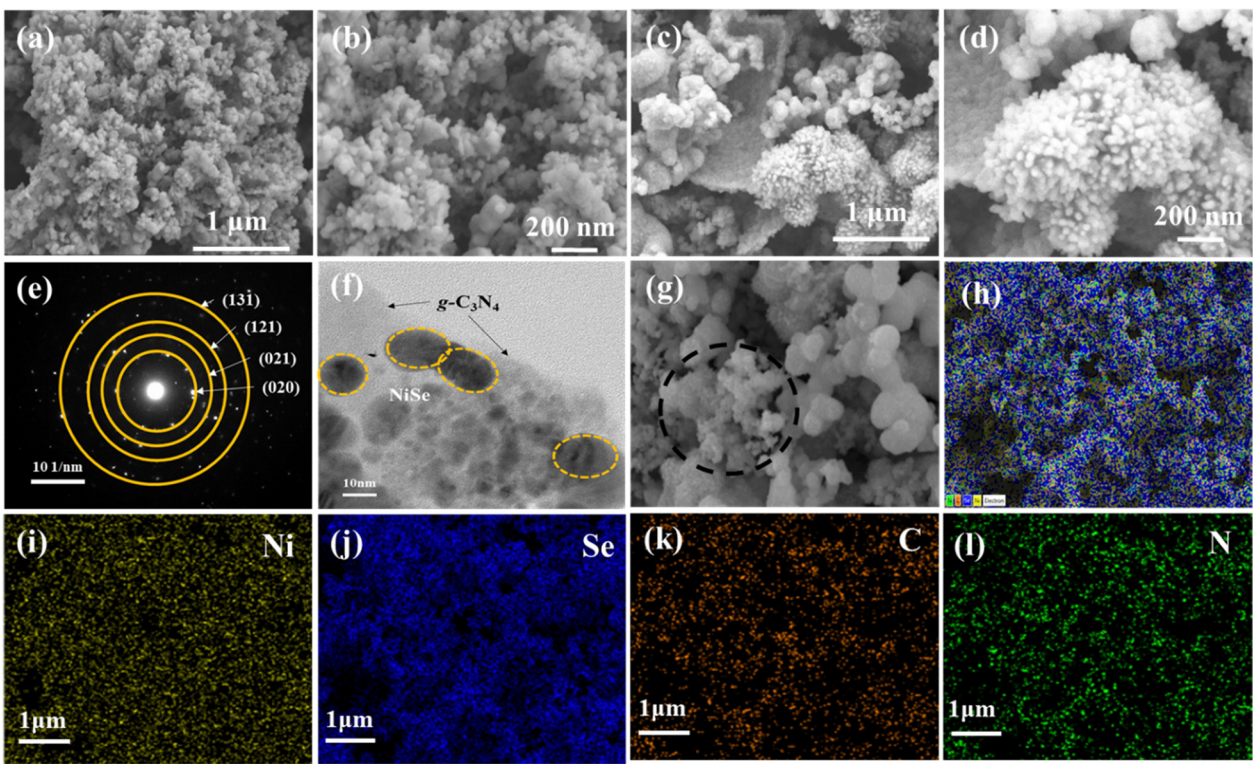

Fig. 2 FE-SEM images of (a), (b) $NiSe_2$, (c), (d) $NiSe_2$/g-C_3N_4, and (e), (f) HR-TEM of $NiSe_2$/g-C_3N_4. (g)–(l) Energy dispersive spectroscopy (EDS) mapping of elements Ni, Se, C, and O in $NiSe_2$/g-C_3N_4.

consist of three peaks at 287.33 eV (N–C═N), 285.51 eV (C–O) and 284.09 eV (C–C). For N 1s spectra, peaks are observed at 400.2 eV (–C–N–H), 399.07 eV (N–C_3), and 397.8 eV (C–N═C). The presence of different functional groups consisting of C and N elements on the surface of the g-C_3N_4 nanosheets could facilitate the ion adsorption and electron transfer required for the HER.[21] The XPS survey spectrum of $NiSe_2$/g-C_3N_4 (Fig. 1(c), (f) and Fig. S1g, ESI†), indicate the existence of Ni, Se, C, and N elements. In the case of $NiSe_2$/g-C_3N_4, Ni 2p peaks are found to be red-shifted when compared to $NiSe_2$ implying that there was electron migration from g-C_3N_4 to $NiSe_2$ and a subsequent charge redistribution around Ni atoms in the composite. This shows the greater synergy between $NiSe_2$ and g-C_3N_4 required for improved HER activity.

The growth and morphology of $NiSe_2$ on the g-C_3N_4 sheets were analyzed by FE-SEM. Fig. 2(a)–(d) show the FE-SEM images of $NiSe_2$ and $NiSe_2$/g-C_3N_4, respectively. The uniformly grown $NiSe_2$ nanoparticles on the g-C_3N_4 nanosheets are seen. These particles are less agglomerated in $NiSe_2$/g-C_3N_4 when compared to $NiSe_2$. This leads to a greater availability of exposed active sites required for electrochemical reactions and ion adsorption during the HER. The structural analysis of the $NiSe_2$/g-C_3N_4 nanocomposite was examined using HR-TEM, and it was clear from this that $NiSe_2$ grains were successfully grown on the g-C_3N_4 nanosheets (Fig. 2(e) and (f)). This direct growth improves the mechanical and chemical stability needed for the increased electrocatalytic activity and stability, which in turn accelerates the ionic/electron transfer. The EDS spectrum of the $NiSe_2$/g-C_3N_4 composite (Fig. 2(g)–(l)) indicates the presence of Ni, Se, C, and N elements in the $NiSe_2$/g-C_3N_4 composite sample. All the elements show peaks at their known energies. The intensity count ratio for Ni and Se was approximately 1 : 2, which implied the presence of $NiSe_2$ in the composite. Fig. S1h (ESI†) displays the EDS elemental mapping for Ni, Se, C, and N in $NiSe_2$/g-C_3N_4 samples. These images reveal the presence of all the elements in the composite, and a homogeneous distribution of $NiSe_2$ on the g-C_3N_4 sheets could be inferred, confirming the successful fabrication of the nanocomposite.

The electrode/electrolyte compatibility is the most crucial for numerous issues that aid the HER performance. Thus, surface wettability becomes significant for the analysis of electrode surface energy and transportation of charges/ions at the interface.[51] To do so, the contact angle, which determines the effective surface energy and hydrophilicity, is used to measure the interaction between electrode surfaces in contact with the electrolyte. The contact angle has an inverse relationship with the surface free energy. From Fig. 3(a), the contact angles of NF, g-C_3N_4/NF, $NiSe_2$/NF, and $NiSe_2$/g-C_3N_4/NF for a 1 M KOH electrolyte are 0°, 113°, 64° and 36° respectively. Thus, the low contact angle of the NiSe/g-C_3N_4 composite implies enhanced wettability.[52,53] The Fowkes' approximation was used to compute the surface free energy.[54,55] A set of four distinct standard liquids (distilled water, ethylene glycol, formamide, and glycerol) with known values of surface tension parameters (polar and dispersion components) were employed for this (see Fig. 3(b)).[56] The calculated surface free energies for g-C_3N_4/NF, $NiSe_2$/NF, and $NiSe_2$/g-C_3N_4/NF were found to be 25.12, 38.49, and 49.2 mJ m^{-2}, respectively (see Fig. 3(c)). The presence of lone pair electrons in g-C_3N_4 enhanced the charge carrier mobility and wettability of the composite. As a result, the reduced contact angle and larger surface energy of the composite electrode aid in the enhancement of the interfacial charge transfer and ion diffusion accessibility.

3.3. Electrochemical studies

A three-electrode configuration was used to measure the HER electrochemical behavior of the synthesized samples. In a typical setup, $NiSe_2$/g-C_3N_4/NF (working), Hg/HgO (reference), and graphite rod (counter) electrodes were used in 1.0 M KOH electrolyte. Further, a comparison was carried out with 20%Pt/C@NF and bare NF to study their HER activity. Fig. 4(a) displays iR-corrected LSV polarization curves measured in the potential range of −0.6 V to 0 *vs.* RHE. The overpotential values were found to be 228, 189, 153, 87, 116, and 64 mV for g-C_3N_4, $NiSe_2$, $NiSe_2$/10g-C_3N_4, $NiSe_2$/20g-C_3N_4, $NiSe_2$/30g-C_3N_4 and 20%Pt/C electrodes, respectively, at a current density of 10 mA cm^{-2}. The $NiSe_2$-based samples demonstrated higher cathodic currents and more positive onset potentials compared to the bare NF indicating the greater HER activities of nickel selenides compared to that of Ni metal. Thus, the HER overpotential for

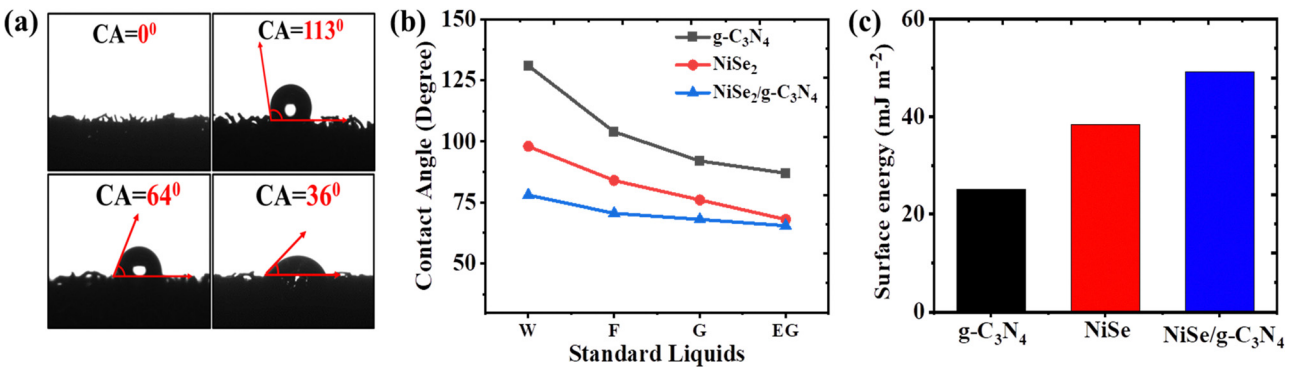

Fig. 3 (a) Contact angle of NF, g-C_3N_4, $NiSe_2$, and $NiSe_2$/g-C_3N_4 electrodes with 6 M KOH solution. (b) The contact angle of g-C_3N_4, $NiSe_2$, and $NiSe_2$/g-C_3N_4 electrodes with distilled water (W), ethylene glycol (EG), glycerol (G), formamide (F) as standard liquids. (c) Surface energy of g-C_3N_4, $NiSe_2$, and $NiSe_2$/g-C_3N_4 electrodes.

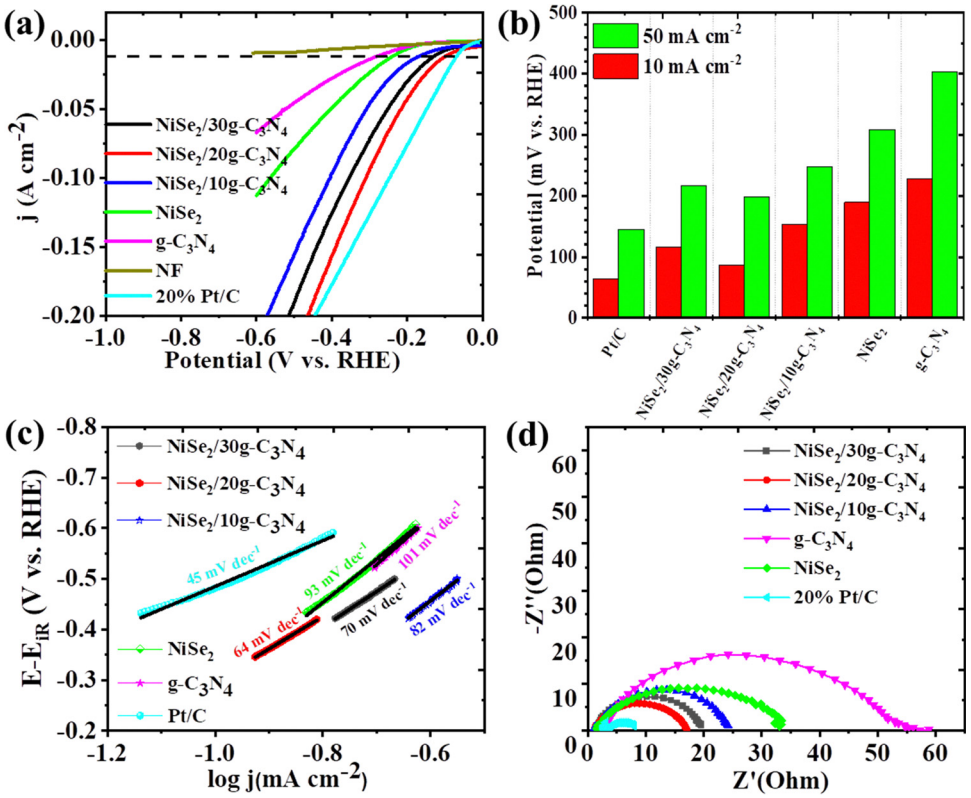

Fig. 4 HER performances (a) LSV, (b) overpotentials, (c) Tafel plots, and (d) Nyquist plot of $NiSe_2$, g-C_3N_4, $NiSe_2$/10g-C_3N_4 $NiSe_2$/20g-C_3N_4, $NiSe_2$/30g-C_3N_4, and 20%Pt/C.

$NiSe_2$/20g-C_3N_4 was just 23 mV more than Pt/C@NF and is the lowest among the prepared samples. Additionally, the overpotentials for all the samples were also measured and compared at a current density of 50 mA cm^{-2} (see Fig. 4(b)). The increase in the current density, increases the overpotential value considerably. The sequence in the decreasing order for the overpotential is g-C_3N_4 > $NiSe_2$ > $NiSe_2$/10g-C_3N_4 > $NiSe_2$/30g-C_3N_4 > $NiSe_2$/20g-C_3N_4, and 20%Pt/C. Thus, compared to the other samples, $NiSe_2$/20g-C_3N_4 exhibits the lowest overpotential and is closer to that of the 20%Pt/C electrode even at a high current density of 50 mA cm^{-2}.

The Tafel slopes derived from related LSV sweeps aid in a better understanding of the HER reaction kinetics (Fig. 4(c)). The Tafel slopes for g-C_3N_4, $NiSe_2$, $NiSe_2$/10g-C_3N_4, $NiSe_2$/20g-C_3N_4, $NiSe_2$/30g-C_3N_4 and 20% Pt/C were calculated to be 103, 93, 82, 64, 70, and 45 mV dec^{-1}, respectively. Pt/C shows the lowest Tafel slope and best HER activity. However, $NiSe_2$/20 g-C_3N_4 shows a lower Tafel slope and an accelerated HER when compared to those of the other samples. The Volmer step serves as a bottleneck for the Volmer–Heyrovsky process in alkaline HER. Thus, heterostructured electrocatalysts with their electronic structure modulation and multiple active sites can promote the adsorption of H_{ad}/OH_{ad} for faster water dissociation in the Volmer step-determined alkaline HER phenomenon.[57] Moreover, the Tafel value is considerably lower than the theoretical Tafel slope of 120 mV dec^{-1} for the Volmer step in alkaline HER, indicating an accelerated water dissociation for $NiSe_2$/20 g-C_3N_4.[49] According to Tafel slope calculations, the synthesized electrocatalyst $NiSe_2$/20g-C_3N_4 follows the Volmer–Heyrovsky mechanism.

Taking into consideration the HER properties, *i.e.* overpotential and Tafel slope, a comparison of our work with that of different research groups, is shown in Table S1 (ESI†). The NiSe@g-C_3N_4 electrode shows the lowest Tafel slope and overpotential amongst all the reported electrocatalysts, suggesting that there is superior HER electrocatalytic activity in an alkaline medium. This high HER catalytic activity of $NiSe_2$/g-C_3N_4 may correspond to the optimum charge transfer kinetics, intrinsic electrode activity, and the presence of several active sites.

EIS measurements help in examining the electrode kinetics. The Nyquist plot helps in the evaluation of R_s (solution resistance) and R_{ct} (charge transfer resistance). The magnitude of R_s is obtained from the *X*-intercept of the Nyquist curve, while R_{ct} is dependent on the diameter of the semi-circle.[58] The low value of R_s implies that there is better electrical integration of the electrode/electrolyte. From Fig. 4(d), it is seen that the diameter of the semi-circle for $NiSe_2$/20g-C_3N_4 is smaller than that of the other samples, which implies there is a lower R_{ct} at the electrode/electrolyte interface during the HER. The R_{ct} values of g-C_3N_4, $NiSe_2$, $NiSe_2$/10g-C_3N_4, $NiSe_2$/20g-C_3N_4, $NiSe_2$/30g-C_3N_4 and 20%Pt/C were calculated to be 55.34, 33.04, 24.17, 17.04, 19.59, and 7.93 Ω, respectively. Thus, NiSe@20g-C_3N_4 shows higher charge transfer kinetics and HER activity compared to the other samples during alkaline water oxidation.

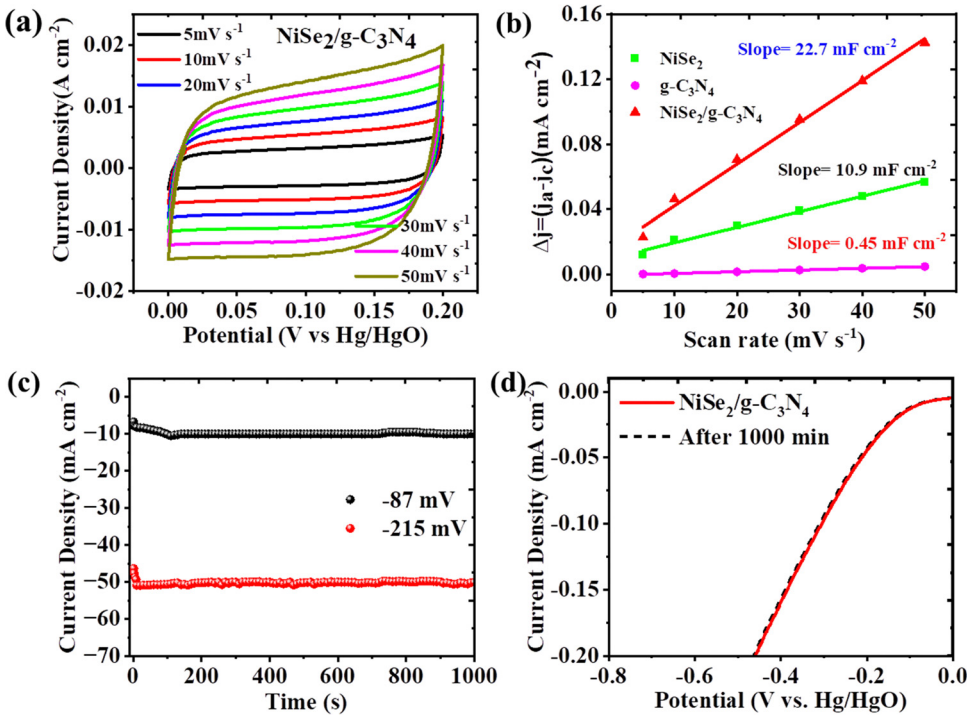

Fig. 5 (a) CV of $NiSe_2$/g-C_3N_4 at 5–50 mV s^{-1} scan rates, (b) estimated values of C_{dl} for g-C_3N_4, $NiSe_2$, and $NiSe_2$/g-C_3N_4. (c) Chronoamperometric measurement at constant potentials −0.087 and 0.215 V *vs.* RHE for $NiSe_2$/g-C_3N_4. (d) LSV curves of $NiSe_2$/g-C_3N_4 before and after 1000 min.

The electrochemical active surface area (ECSA) was determined using scan rate-dependent normalized CV-derived C_{dl} measurements in the non-faradaic region. The C_{dl} values for g-C_3N_4, $NiSe_2$, and $NiSe_2$/20g-C_3N_4, were computed to be 6.45, 10.9 and 22.7 mF cm^{-2}, respectively, (Fig. 5(a), (b), and Fig. S2b–d, ESI†). Thus, $NiSe_2$/20g-C_3N_4 displayed a C_{dl} which is greater than that of bare $NiSe_2$ and g-C_3N_4. Accordingly, the ECSA of g-C_3N_4, $NiSe_2$, and $NiSe_2$/20g-C_3N_4 electrodes were calculated to be 161.25, 275.5, and 567.5 cm^{-2}, respectively. It is also seen that the C_{dl} and ECSA values of NiSe@20g-C_3N_4 are higher than those of other samples. This implies that NiSe@g-C_3N_4 has the highest density of HER active sites. The turnover frequency (TOF) was calculated to study the intrinsic activity. The TOF values for $NiSe_2$, and $NiSe_2$/20g-C_3N_4 were found to be 0.054 and 0.085 s^{-1}, respectively. A TOF value of 0.085 s^{-1} means that 85 hydrogen molecules are produced per second per active site.[59] Thus, the intrinsic activity for $NiSe_2$/20g-C_3N_4 was the highest among all the prepared samples.

For commercial scale-up of hydrogen production using water decomposition, in addition to high performance, the long-term stability also becomes significant. The chronoamperometry measurements were carried out for $NiSe_2$/g-C_3N_4 electrode at two different potentials *i.e.* 87 and 215 mV *vs.* RHE for a time interval of 1000 min. Fig. 5(c) demonstrates that the current density fairly remains constant even after 1000 min of HER, which explains the long-term durability of the electrode. This stability is higher when compared to that of the bare $NiSe_2$ and g-C_3N_4 electrodes (see Fig. S2a, ESI†). Moreover, LSV curves did not change significantly even after 1000 min of the experiment (Fig. 5(d)), suggesting the potential of $NiSe_2$/g-C_3N_4 for long-run applications. As a consequence, the enhanced electrocatalytic performance of $NiSe_2$/g-C_3N_4 over bare $NiSe_2$ and g-C_3N_4 is the result of the modified surface chemistry generated by g-C_3N_4 and tailored electronic characteristics of the composite. Thus, the optimal loading of 20g-C_3N_4 in the $NiSe_2$ composite showed an enhanced synergistic interaction and provided a balance between active sites and electron transfer pathways, thus enhancing the charge transfer kinetics and HER activity. This loading also provided an optimal surface area, facilitating efficient mass/charge transport, while promoting a favorable electronic structure that optimized the adsorption and activation of hydrogen intermediates during the HER process.

4. Conclusion

In summary, the synthesis of a $NiSe_2$/g-C_3N_4 nanocomposite using a simple hydrothermal technique was carried out. The composite electrode demonstrated high HER catalytic activity in 1 M KOH aqueous solution. The Tafel slope and overpotential values for $NiSe_2$/g-C_3N_4 were less than those for the $NiSe_2$ and g-C_3N_4 electrodes. The nanocomposite shows excellent performance which is close to that of the Pt/C catalyst. Moreover, long term stability for 1000 min without performance decline was achieved. A stronger $NiSe_2$ catalyst supported by the g-C_3N_4 interface arises primarily due to *in situ* growth and higher chemical stability. The electrochemical tests and analysis reveal that improved intrinsic catalytic activity, larger ECSA, lowered contact angle, and faster charge kinetics contribute to

the excellent catalytic performance. This study sheds light on the development of a high-performance, long-term stable, noble-metal-free electrocatalyst for use in the HER.

Data availability

Data will be made available on request.

Author contributions

Somnath R. Khaladkar: conceptualization, data curation, formal analysis, investigation, validation, visualization, writing – original draft. Oshnik Maurya: data curation, formal analysis, writing – original draft. Girish Gund: validation, visualization, writing – review and editing. Bhavesh Sinha: writing – review and editing. Girish Kamble: data curation. Jin Hyeok Kim: resources, project administration, supervision, funding acquisition. R. R. Deshmukh: project administration, resources, writing – review and editing. Archana Kalekar: conceptualization, funding acquisition, investigation, project administration, resources, supervision, writing – review and editing.

Conflicts of interest

There are no conflicts to declare.

Acknowledgements

The funding for Dr Archana Kalekar research is provided by SERB [EEQ/2022/001076]. Dr Girish Gund acknowledges the DST-SERB [SRG/2021/001791] for their funding. Somnath R. Khaladkar and Oshnik Maurya acknowledge their financial support from the UGC NET-JRF (517906) and UGC NFOBC (202021-201610071195), respectively. This work was also supported by a National Research Foundation of Korea (NRF) grant funded by the government of the Republic of Korea (MSIT) (no. 2022R1A2C2007219). Moreover, this work was supported by the Priority Research Centers Program of the National Research Foundation of Korea (NRF) funded by the Ministry of Education, Science, and Technology (2018R1A6A1A03024334).

References

1 O. Maurya, S. R. Khaladkar, B. Sinha, B. M. Bhanage, R. R. Deshmukh, J. H. Kim and A. Kalekar, *Electrochim. Acta*, 2023, **471**, 143391.
2 S. Lavate, H. P. S. Yalamati and R. Srivastava, in *Solar-Driven Green Hydrogen Generation and Storage*, ed. R. Srivastava, J. Chattopadhyay and D. M. F. Santos, Elsevier, 2023, pp.507–524.
3 N. Kumar, M. Rehan, S. Khaladkar, O. Maurya, K. Rao, A. Kalekar, M. Kumar and J. Kumar, *Mater. Chem. Phys.*, 2024, **316**, 129072.
4 O. Maurya, S. Khaladkar, M. R. Horn, B. Sinha, R. Deshmukh, H. Wang, T. Y. Kim, D. P. Dubal and A. Kalekar, *Small*, 2021, **17**, 1–29.
5 S. Khaladkar, G. Gund, O. Maurya, B. Sinha, P. Salame, D. Dubal, R. Deshmukh and A. Kalekar, *Adv. Energy Sustainability Res.*, 2023, 2300013.
6 J. B. M. Parambath, N. Hussain, H. Alawadhi, Y. Park, D. D. Dionysiou, C. Han and A. A. Mohamed, *Comments Inorg. Chem.*, 2022, **42**, 249–270.
7 R. R. Deshmukh, A. S. Kalekar, S. R. Khaladkar and O. C. Maurya, in *Nanotechnology for Energy and Environmental Engineering*, ed. L. Ledwani and J. S. Sangwai, Springer International Publishing, Cham, 2020, pp.329–354.
8 M. R. Ansari, S. Khaladkar, A. Kalekar, M.-D. Kim and K. R. Peta, *J. Energy Storage*, 2023, **74**, 109494.
9 S. Shen, H. Zhang, K. Song, Z. Wang, T. Shang, A. Gao, Q. Zhang, L. Gu and W. Zhong, *Angew. Chem., Int. Ed.*, 2024, **63**, e202315340.
10 X. Wang, Y. Fei, J. Chen, Y. Pan, W. Yuan, L. Y. Zhang, C. X. Guo and C. M. Li, *Small*, 2022, **18**, 2103866.
11 X. Wang, Y. Fei, W. Wang, W. Yuan and C. M. Li, *ACS Appl. Energy Mater.*, 2019, **2**, 8851–8861.
12 S. Bama Sundararaj, S. Tamilarasan, K. Kadirvelu and S. Thangavelu, *Appl. Surf. Sci.*, 2023, **612**, 155785.
13 Z. Wang, Z. Lin, Y. Wang, S. Shen, Q. Zhang, J. Wang and W. Zhong, *Adv. Mater.*, 2023, **35**, 1–8.
14 N. Sahu, J. K. Das and J. N. Behera, *Inorg. Chem.*, 2022, **61**, 2835–2845.
15 W. Yuan, Y. Li, L. Liang, F. Wang and H. Liu, *ACS Appl. Energy Mater.*, 2022, **5**, 5036–5043.
16 Z. Tian, Y. Liu, Q. Xu, Y. Shi, C. Ma, B. Peng, G. Liu, J. Yang and W. Zheng, *Electrochim. Acta*, 2022, **425**, 140711.
17 K. Song, H. Zhang, Z. Lin, Z. Wang, L. Zhang, X. Shi, S. Shen, S. Chen and W. Zhong, *Adv. Funct. Mater.*, 2023, **2312672**, 1–9.
18 X. Fan, X. Wang, W. Yuan and C. M. Li, *Sustainable Energy Fuels*, 2017, **1**, 2172–2180.
19 Y. Chen, B. Zhang, Y. Liu, J. Chen, H. Pan and W. Sun, *Mater. Today Catal.*, 2023, **1**, 100003.
20 S. R. Khaladkar, O. Maurya, G. Gund, B. Sinha, D. Dubal, R. R. Deshmukh and A. Kalekar, *J. Energy Chem.*, 2023, **87**, 304–313.
21 K. Li, Z. Shi, L. Wang, W. Wang, Y. Y. Liu, H. Cheng, Y. Yang and L. Zhang, *J. Hazard. Mater.*, 2023, **448**, 130890.
22 S. R. Khaladkar, O. Maurya, G. Gund, B. Sinha, D. Dubal, R. Deshmukh and A. Kalekar, *ACS Appl. Mater. Interfaces*, 2024, **16**(9), 11408–11420.
23 M. Guan, C. Wang, S. Li, H. Du and Y. Yuan, *ACS Sustainable Chem. Eng.*, 2020, **8**, 10313–10320.
24 M. Zulqarnain, A. Shah, M. A. Khan, F. Jan Iftikhar and J. Nisar, *Sci. Rep.*, 2020, **10**, 1–8.
25 S. Yousefzadeh and N. Morovati, *Int. J. Hydrogen Energy*, 2020, **45**, 33512–33520.
26 X. Lv, W. Wei, H. Wang, B. Huang and Y. Dai, *Appl. Catal., B*, 2020, **264**, 118521.
27 J. Jia, W. Sun, Q. Zhang, X. Zhang, X. Hu, E. Liu and J. Fan, *Appl. Catal., B*, 2020, **261**, 118249.

28 Z. Zhuang, Y. Li, Z. Li, F. Lv, Z. Lang, K. Zhao, L. Zhou, L. Moskaleva, S. Guo and L. Mai, *Angew. Chem., Int. Ed.*, 2018, **57**, 496–500.
29 H. Jin, X. Liu, Y. Jiao, A. Vasileff, Y. Zheng and S. Z. Qiao, *Nano Energy*, 2018, **53**, 690–697.
30 J. Liang, Y. Zheng, J. Chen, J. Liu, D. Hulicova-Jurcakova, M. Jaroniec and S. Z. Qiao, *Angew. Chem., Int. Ed.*, 2012, **51**, 3892–3896.
31 R. Shwetharani, S. Kapse, R. Thapa, D. H. Nagaraju and R. G. Balakrishna, *ACS Appl. Energy Mater.*, 2020, **3**, 12682–12691.
32 G. Dong, H. Fan, K. Fu, L. Ma, S. Zhang, M. Zhang, J. Ma and W. Wang, *Composites, Part B*, 2019, **162**, 369–377.
33 Y. Liu, Y. Zheng, Q. Xu, Y. Shi, Z. Tian, R. wang, G. Zhang, J. Chen, Z. Wang and W. Zheng, *Chem. Eng. J.*, 2020, **387**, 124121.
34 Z. Chen, Y. Gao, F. Chen and H. Shi, *Chem. Eng. J.*, 2021, **413**, 127474.
35 H. Cölfen and S. Mann, *Angew. Chem., Int. Ed.*, 2003, **42**, 2350–2365.
36 B. Z. Zhang, H. Sun, X. Shao, D. Li, H. Yu and M. Han, *Adv. Mater.*, 2005, **17**, 42–47.
37 X. Wang, W. Mao, J. Zhang, Y. Han, C. Quan, Q. Zhang, T. Yang, J. Yang, X. Li and W. Huang, *J. Colloid Interface Sci.*, 2015, **448**, 17–23.
38 J. Safaei, N. A. Mohamed, M. F. Mohamad Noh, M. F. Soh, N. A. Ludin, M. A. Ibrahim, W. N. Roslam Wan Isahak and M. A. Mat Teridi, *J. Mater. Chem. A*, 2018, **6**, 22346–22380.
39 J. Kavil, P. M. Anjana, P. Periyat and R. B. Rakhi, *Sustainable Energy Fuels*, 2018, **2**, 2244–2251.
40 G. K. Subhash, M. D. Benoy, J. Duraimurugan, S. Prabhu, R. Siranjeevi, R. Ramesh, G. Suresh kumar and M. Shkir, *Inorg. Chem. Commun.*, 2022, **142**, 109719.
41 F. Shiravani, J. Tashkhourian and B. Haghighi, *Sustainable Energy Fuels*, 2021, **5**, 3229–3239.
42 T. Ivanova, A. Harizanova, M. Shipochka and P. Vitanov, *Materials*, 2022, **15**, 1742.
43 S. Wang, P. He, L. Jia, M. He, T. Zhang, F. Dong, M. Liu, H. Liu, Y. Zhang, C. Li, J. Gao and L. Bian, *Appl. Catal., B*, 2019, **243**, 463–469.
44 D. Sun, J. Zhang, H. Ren, Z. Cui and D. Sun, *J. Phys. Chem. C*, 2010, **114**, 12110–12116.
45 J. Nai, X. Xu, Q. Xie, G. Lu, Y. Wang, D. Luan, X. Tao and X. W. Lou, *Adv. Mater.*, 2022, **34**, 1–7.
46 B. Jansi Rani, G. Ravi, R. Yuvakkumar, B. Saravanakumar, M. Thambidurai, C. Dang and D. Velauthapillai, *ACS Omega*, 2020, **5**, 14702–14710.
47 S. Manickam, H. Kuzhandaivel, Y. Selvaraj, M. C. Franklin and K. Sivalingam Nallathambi, *Dalton Trans.*, 2022, **51**, 1542–1552.
48 I. Ahmad, S. B. Khan, T. Kamal and A. M. Asiri, *J. Mol. Liq.*, 2017, **229**, 429–435.
49 Y. Bai, H. Zhang, X. Lu, L. Wang, Y. Zou, J. Miao, M. Qiao, Y. Tang and D. Zhu, *Chem. – Eur. J.*, 2023, **29**(28), 0947–6539, DOI: **10.1002/chem.202300205**.
50 L. Zhao, Y. Zhang, Z. Zhao, Q. H. Zhang, L. B. Huang, L. Gu, G. Lu, J. S. Hu and L. J. Wan, *Natl. Sci. Rev.*, 2020, **7**, 27–36.
51 M. M. Vadiyar, S. C. Bhise, S. K. Patil, S. S. Kolekar, A. R. Shelke, N. G. Deshpande, J. Y. Chang, K. S. Ghule and A. V. Ghule, *Chem. Commun.*, 2016, **52**, 2557–2560.
52 H. S. Lee, G. S. Gund and H. S. Park, *J. Power Sources*, 2020, **451**, 227763.
53 T. Liu, K. Wang, Y. Chen, S. Zhao and Y. Han, *Green Energy Environ.*, 2019, **4**, 171–179.
54 F. M. Fowkes, *J. Phys. Chem.*, 1963, **67**, 2538–2541.
55 F. M. Fowkes, *J. Adhes. Sci. Technol.*, 1987, **1**, 7–27.
56 R. R. Deshmukh and A. R. Shetty, *J. Appl. Polym. Sci.*, 2008, **107**, 3707–3717.
57 X. Ma, J. Yang, X. Xu, H. Yang and C. Peng, *RSC Adv.*, 2021, **11**, 34432–34439.
58 N. O. Laschuk, E. B. Easton and O. V. Zenkina, *RSC Adv.*, 2021, **11**, 27925–27936.
59 K. S. Ranjith, S. Y. Lee, S. M. Ghoreishian, N. R. Chodankar, G. S. Rama Raju, S. J. Patil, Y. S. Huh, S. J. Park and Y. K. Han, *Carbon N. Y.*, 2023, **206**, 246–259.